nature physics

ARTICLES

https://doi.org/10.1038/s41567-019-0464-1

Actin dynamics drive cell-like membrane deformation

Camille Simon[1,2,6], Rémy Kusters[1,2,6], Valentina Caorsi[1,2,6], Antoine Allard[1,2,3], Majdouline Abou-Ghali[1,2], John Manzi[1,2], Aurélie Di Cicco[1,2], Daniel Lévy[1,2], Martin Lenz[4], Jean-François Joanny[1,2,5], Clément Campillo[3], Julie Plastino[1,2], Pierre Sens[1,2,7*] and Cécile Sykes[1,2,7*]

Cell membrane deformations are crucial for proper cell function. Specialized protein assemblies initiate inward or outward membrane deformations that the cell uses respectively to uptake external substances or probe the environment. The assembly and dynamics of the actin cytoskeleton are involved in this process, although their detailed role remains controversial. We show here that a dynamic, branched actin network is sufficient to initiate both inward and outward membrane deformation. The polymerization of a dense actin network at the membrane of liposomes produces inward membrane bending at low tension, while outward deformations are robustly generated regardless of tension. Our results shed light on the mechanism cells use to internalize material, both in mammalian cells, where actin polymerization forces are required when membrane tension is increased, and in yeast, where those forces are necessary to overcome the opposing turgor pressure. By combining experimental observations with physical modelling, we propose a mechanism that explains how membrane tension and the architecture of the actin network regulate cell-like membrane deformations.

Many cell functions rely on the ability of cells to change their shape. The deformation of the cell membrane is produced by the activity of various proteins that curve the membrane inwards or outwards, by exerting pulling and pushing forces or by imposing membrane curvature via structural effects. When cells take up external material, it is often associated with membrane invaginations followed by vesicle transport. This process is called endocytosis. Such inward deformation of the cell membrane can be initiated by specific proteins, such as clathrin, which coat the membrane and impose geometrical constraints that bend the membrane inwards. In this view, the action of the actin cytoskeleton, a filamentous network that forms at the membrane, is crucial only at a later stage for membrane elongation. Nevertheless, correlation methods revealed unambiguously that, in yeast, membrane bending is not triggered by the presence of coat proteins, but by a dynamic actin network formed at the membrane through the Arp2/3 complex branching agent[1–3]. In mammalian cells, clathrin-mediated endocytosis requires the involvement of actin if the plasma membrane is tense (for example, following osmotic swelling or mechanical stretching[4]). However, the exact mechanism of membrane deformation in this process is still poorly understood. Strikingly, the same type of branched actin network is able to bend the membrane the other way in, creating outward-pointing membrane deformations, called dendritic filopodia. These structures are precursors of dendritic spines in neurons, and essential for signal transmission[5]. Dendritic filopodia differ from conventional filopodia, localized at the leading edge of the cell, where actin filaments are parallel. Whereas the pioneering work of Liu et al.[6] already established how thin filopodia form by bundling actin filaments, the production of a dendritic filopodia-like membrane protrusion containing a branched actin network has never been investigated.

How the same branched actin structure can be responsible for the initiation of filopodia, which are outward-pointing membrane deformations, as well as endocytic invaginations that deform the membrane inward is what we want to address in this paper. Such a question is difficult to investigate in cells that contain redundant mechanisms for cell deformation. Actin dynamics triggered at a liposome membrane provide a control on experimental parameters such as membrane composition, curvature and tension, and allow the specific role of actin dynamics to be addressed. We unambiguously show that the same branched actin network is able to produce both endocytosis-like and dendritic filopodia-like deformations. With a theoretical model, we predict under which conditions the stress exerted on the membrane will lead to inward- and/or outward-pointing membrane deformations. Combining experiments and theory allows us to decipher how the interplay between membrane tension, actin dynamics and actin network structure produces inward or outward membrane deformations.

Membrane tubes and spikes

Liposomes are covered with an activator of the Arp2/3 complex, pVCA, the proline-rich domain–verprolin homology–central–acidic sequence from human WASP, which is purified with a streptavidin tag, and that we call hereafter S-pVCA. A branched actin network grows at their surface when placed in a mixture containing monomeric actin, profilin the Arp2/3 complex and capping protein (CP) ('reference condition', Methods and Fig. 1a). Strikingly, the membrane of liposomes is not smooth, but instead displays a rugged profile: membrane tubes, hereafter called 'tubes', radiate from the liposome surface and extend into the actin network (Fig. 1b), even when comet formation has occurred[7,8] (Supplementary Fig. 1a). The initiation of these tubes is reminiscent of the early stage of

[1]Laboratoire Physico Chimie Curie, Institut Curie, PSL Research University, CNRS UMR168, Paris, France. [2]Sorbonne Universités, UPMC Univ. Paris 06, Paris, France. [3]LAMBE, Université Evry, CNRS, CEA, Université Paris-Saclay, Evry, France. [4]LPTMS, CNRS, Univ. Paris-Sud, Université Paris-Saclay, Orsay, France. [5]ESPCI-Paris, Paris, France. [6]These authors contributed equally: Camille Simon, Rémy Kusters, Valentina Caorsi. [7]These authors jointly supervised this work: Pierre Sens, Cécile Sykes. *e-mail: pierre.sens@curie.fr; cecile.sykes@curie.fr

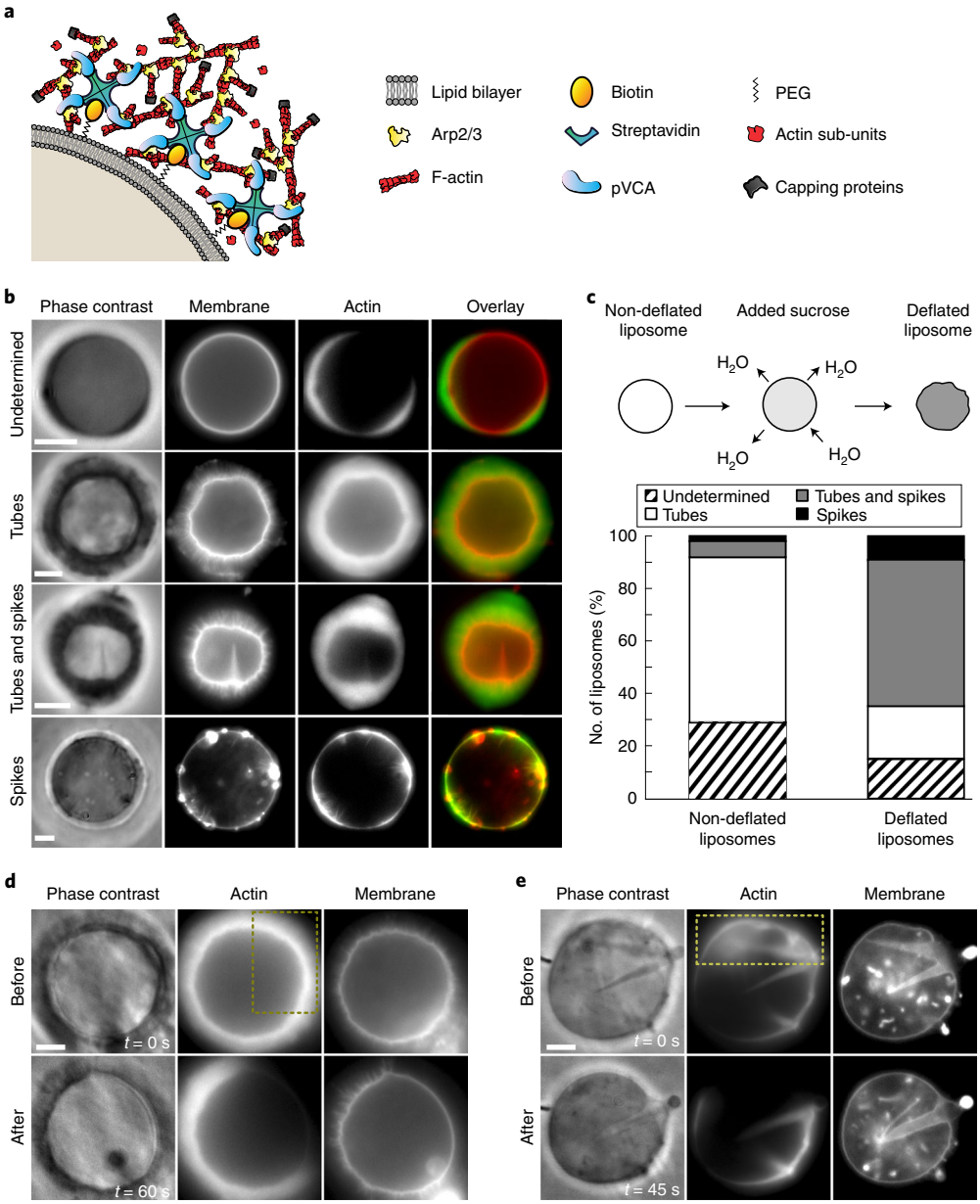

Fig. 1 | Experimental system and observations. a, Scheme of the experimental system; proteins not to scale. **b**, Membrane deformations in both non-deflated (first three rows) and deflated conditions (last row). **c**, Top: liposome deflation. Bottom: number of liposomes displaying different indicated behaviours. Non-deflated liposomes, $n = 311$. Deflated liposomes, $n = 123$. **d**,**e**, Actin network photo-damage (yellow dashed rectangle) on a liposome displaying membrane tubes (**d**) or spikes (**e**). Phase-contrast and epifluorescence microscopy of membrane (Texas Red-DHPE, red) and actin network (actin–Alexa Fluor 488, green). All scale bars, 5 μm.

endocytosis. Interestingly, some liposomes display another type of membrane deformation, characterized by a conical shape (hereafter referred to as 'spikes') that points towards the liposome interior (Fig. 1b); these spikes are reminiscent of dendritic filopodia structures in cells. Some of the liposomes carry both tubes and spikes, while others are 'undetermined', as no membrane deformation is visually detectable (Fig. 1b). Spikes have a wide base of a few micrometres and a length that spans at least half of the liposome diameter. In contrast, tubes are thin, with a diameter under the resolution limit of optical microscopy (less than a few hundred nanometres). When membrane tension is unaffected, 63.0% of liposomes display only tubes, 2.3% only spikes, while 6.1% of liposomes carry a mix of both, and 28.6% are undetermined (Fig. 1c, non-deflated liposomes). To examine how membrane tension affects the occurrence of tubes and spikes, liposomes are deflated by a hyper-osmotic shock (Methods) before actin polymerization is triggered. This treatment leads to a huge increase in the number of liposomes displaying spikes: 65.0% of deflated liposomes display spikes (with or without tubes), compared to 8.4% in non-deflated conditions (Fig. 1c, $P < 0.0001$). Yet, the frequency with which tubes (with or without spikes) are observed is essentially unaffected: 69.1% for non-deflated liposomes compared to 74.8% for deflated liposomes (not significant, $P = 0.24 > 0.05$, Supplementary Fig. 1b). An increase in membrane tension by a hypo-osmotic treatment (Methods) does not change the occurrence of tubes and spikes significantly (Supplementary Fig. 1c).

Membrane tubes and spikes exclusively rely on the presence of the actin network, as they disappear when the network is destructed[7]

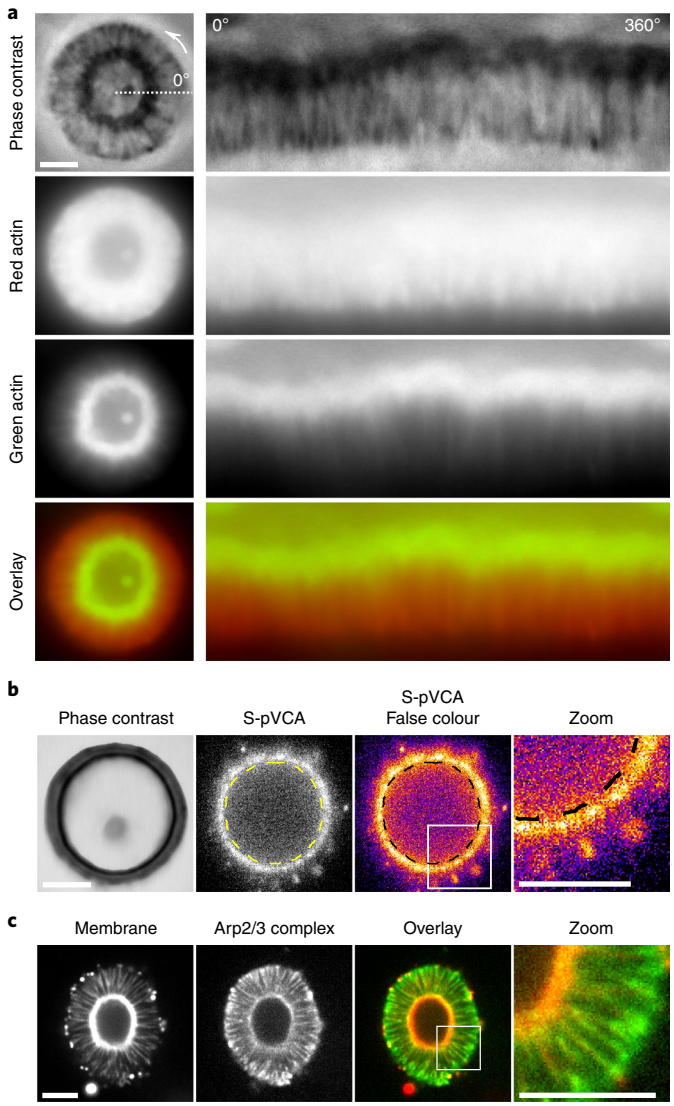

Fig. 2 | Actin incorporation during tube formation. a, Left: a red actin network is grown for 20 min, and then an excess of green actin is added, so green regions indicate newly polymerized actin. Right: corresponding polar plots. **b**, Activator of actin polymerization, S-pVCA. False-colour image and zoom in (white rectangle); the membrane is indicated with a dashed line. **a**,**b**, Phase-contrast and epifluorescence microscopy of the actin network labelled with Alexa Fluor 568 (red) and Alexa Fluor 488 (green) (**a**), and of S-pVCA–Alexa Fluor 546 (**b**). **c**, Confocal images of labelled membrane (Texas Red-DHPE, red) and the Arp2/3 complex (Alexa Fluor 488 C_5-maleimide, green) and zoom in (white rectangle). All scale bars, 5 µm.

(Fig. 1d,e and Methods). A possible effect of membrane pre-curvature induced by pVCA attachment to the membrane is ruled out (Supplementary Information and Supplementary Fig. 2).

Characterization of tubes

To assess where new actin monomers are incorporated during tube growth, we incorporate differently labelled monomers (green) after 20 min (Methods). As previously observed for actin networks growing around polystyrene beads[9,10], new monomers insert at the liposome surface (Fig. 2a). Strikingly, new (green) monomers are also observed within the already grown (red) actin network (Fig. 2a), indicating new actin incorporation on the sides of membrane tubes (tubes are evidenced by phase-contrast imaging, Fig. 2a, top). This observation is confirmed by the localization, along tubes and at the liposome surface, of S-pVCA (Fig. 2b), the Arp2/3 complex (Fig. 2c) and free barbed ends (Supplementary Fig. 3). Moreover, the presence of the Arp2/3 complex everywhere in the whole volume of the actin network demonstrates its dentritic nature (Fig. 2c).

We find that the average length of the longest tubes increases linearly with network thickness (Fig. 3a,b). In fact, maximal tube length roughly equals the thickness of the actin network, independently of membrane tension (Fig. 3b, slope 0.89 ± 0.04), albeit deflated liposomes produce a smaller actin cortex. Moreover, we find that tubes grow simultaneously with the actin network (Fig. 3c,d and Supplementary Fig. 4). Tubes shorter than the network thickness are also present, as evidenced by confocal microscopy (Supplementary Fig. 5a).

The origin of the accumulation of membrane fluorescence detected at the tip of some of the longer tubes is unclear. We observe that S-pVCA forms aggregates on membranes and sticks membranes together, even in the absence of actin (Supplementary Fig. 6). It is possible that small vesicles are attached via S-pVCA to the membrane before polymerization starts and are pushed outward by actin growth. However, the presence of different tube lengths (Supplementary Fig. 5) rules out the possibility that tubes could be formed only by pre-existing attached vesicles.

Characterization of spikes

We find that new actin is incorporated at the tips of the spikes as well as at the sides (Fig. 4a), consistent with the localization of S-pVCA (Fig. 4b). Spikes are filled with the Arp2/3 complex and CP (Fig. 4c and Supplementary Fig. 7), characteristic of a branched network. A clump of actin is observable at the base of the spikes (Fig. 4d). The thickness of the clump bears no clear correlation with the length of the spikes (Supplementary Fig. 8a), but slightly correlates with their width (Supplementary Fig. 8b). Spikes initially elongate with time until polymerization slows down; the basal width of spikes, however, remains roughly constant over time (Fig. 4e and Supplementary Fig. 8c).

Effect of network mesh size and membrane tension

Lowering the Arp2/3 complex or CP concentrations could, in principle, result in loosening the network, but fails to form a cohesive thick enough (>500 nm) network[11]. Using the property of profilin to inhibit branching and therefore loosen the actin network[12], we obtain a visible, thick, network comparable to reference conditions (Supplementary Fig. 9a and Methods). We find that the occurrence of tubes is reduced in these conditions (74.8% of liposomes display tubes when profilin is in excess compared to 91.4% in reference conditions, Supplementary Fig. 9b, $P < 0.0001$). Strikingly, decreasing membrane tension in loosened network conditions significantly increases the presence of tubes and spikes (Supplementary Fig. 9b, $P < 0.0001$).

Theoretical models for spikes and tubes

The appearance of large-scale membrane deformations (spikes) driven by a uniformly polymerizing actin network is rationalized using analytical modelling and numerical finite-element calculations (Methods). The actin network behaves as a viscoelastic material with an elastic behaviour at short time and a viscous behaviour at long time due to network rearrangement, the crossover time being on the order of 1–10 s (refs. [13–15]). We focus on the viscous behaviour as the growth of the network occurs on timescales of tens of minutes.

We model the growth of the actin network with a uniform actin polymerization velocity v_g normal to the liposome membrane (motivated by Fig. 4a) and solve the hydrodynamic force balance equation at low Reynolds number (the 'Stokes equation') (Methods). Actin polymerization on a flat membrane results

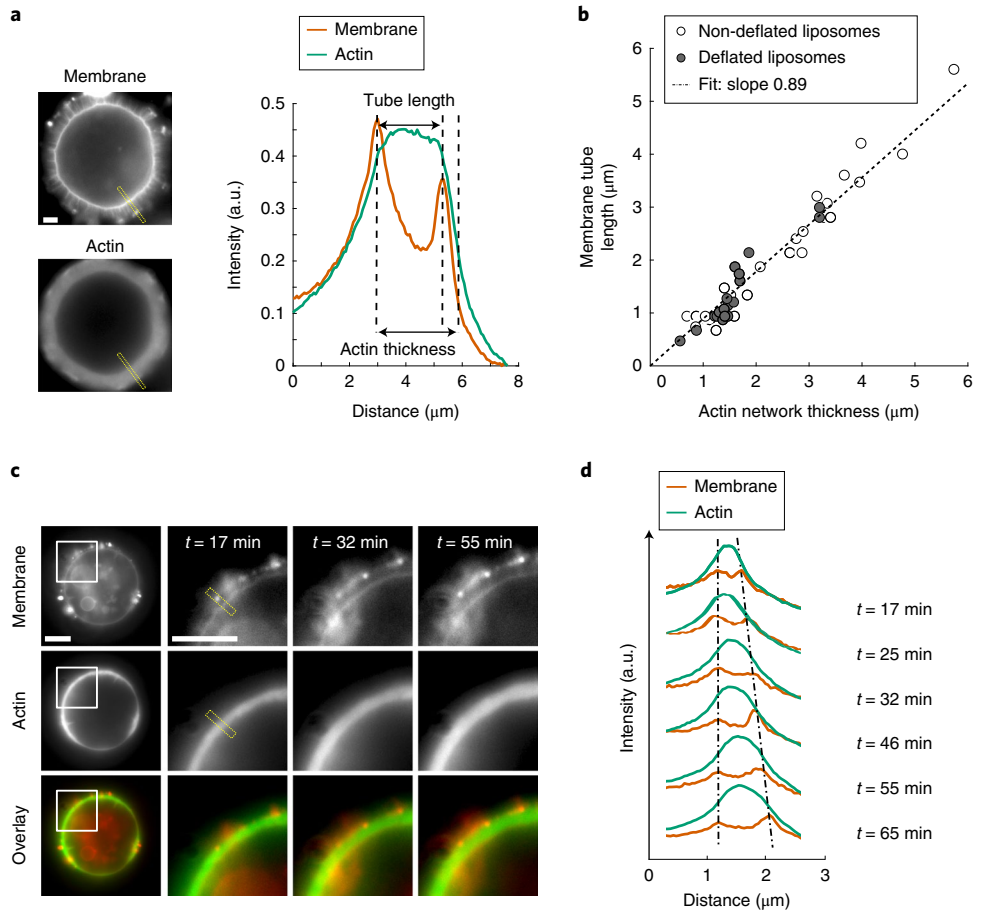

Fig. 3 | Tube length compared to network thickness. a, Tube length and actin network thickness are measured from fluorescence intensity profiles (yellow dashed box) of the membrane (Texas Red-DHPE, red) and the actin (Alexa Fluor 488, green) channels (Methods). **b**, Tube length as a function of actin network thickness. White circles: non-deflated liposomes. Grey circles: deflated liposomes. **c**, Dynamics of tube growth (times indicate elapsed time from the start of actin polymerization). **d**, Fluorescence profile of the yellow dashed boxes shown in **c**. Membrane and actin fluorescence intensities plotted over time (indicated). Other examples are shown in Supplementary Fig. 4. **a**,**c**, Epifluorescence microscopy of membrane (Texas Red-DHPE, red) and actin (Alexa Fluor 488, green). All scale bars, 5 μm.

in a uniform actin flow that does not generate any mechanical stress. Small perturbations of membrane shape modulate the actin velocity field and generate viscous stress on the membrane. For a periodic deformation (Fig. 5a, left), the actin stress varies as the square of the deformation amplitude (Methods) in agreement with actin growth on a curved surface[13,16]. For a localized (Gaussian) membrane perturbation $u(x) = Ae^{-(x/b)^2}$ with amplitude A and width b (Fig. 5a, right), we calculate the pressure and velocity fields in the actin layer numerically (Fig. 5b). Velocity gradients in the growing actin layer, generated by the deformed surface, induce a normal pushing force at the centre of the perturbation, and pulling forces at the periphery of the perturbation (Fig. 5c), that amount to a zero net force when integrated over the deformation area. This contrasts with existing models of filopodia formation, which usually consider bundled actin filaments exerting a net pushing force on the membrane that do not precisely address the force balance within the actin network[6,17,18]. Here, we do not a priori distinguish the detailed structure of the actin network at the membrane from the one in the protrusion, treating the actin network as a continuum.

A scaling analysis of the Stokes equation, confirmed by our numerical calculation, leads to a normal stress at the centre of the perturbation ($x=0$) that scales as $\sigma_{nn} \approx -\eta A^2 b^{-3} v_g$, where η is the viscosity of the actin layer (Supplementary Fig. 10a,b). An intuitive understanding of this scaling behaviour is given in the Supplementary Information.

The normal stress σ_{nn} is balanced by the membrane elastic restoring stress[19] $\sigma_{memb} = -\gamma C + \kappa\ \partial_s^2 C$, where γ is the membrane tension, κ is the bending rigidity, C is the membrane curvature ($\sim A/b^2$) and ∂_s the curvilinear derivative ($\sim 1/b$). Considering that b is larger than the characteristic length $\gamma = \sqrt{\kappa/\gamma}$, the stress is dominated by membrane tension. The balance of actin polymerization and membrane stresses defines a threshold amplitude $A^* = \gamma b/(\eta v_g)$. When the amplitude of the perturbation is smaller than this threshold ($A < A^*$) the membrane stress dominates and the perturbation relaxes. Above the threshold ($A > A^*$) the force exerted by the network is dominant and the instability develops. We now evaluate whether such a perturbation could be reached by thermal fluctuations characterized by the Boltzmann constant k_B and the temperature T. The average membrane thermal roughness at length scales larger than the actin mesh size ξ, characterized by the average of the gradient of the membrane shape ∇h, is given by $<|\nabla h|^2> \sim \frac{k_B T}{4\pi\kappa} \log\left(\left(\frac{2\pi\lambda}{\xi}\right)^2 + 1\right)$ (ref. [19]). Identifying $<|\nabla h|^2>$ with $(A/b)^2$ (provided λ and ξ are on the same order), spikes are predicted below a threshold tension: $\gamma^* \approx \eta v_g \sqrt{k_B T/(4\pi\kappa)}$. Evaluating actin network viscosity η as the product of the elastic modulus (E) times the viscoelastic relaxation

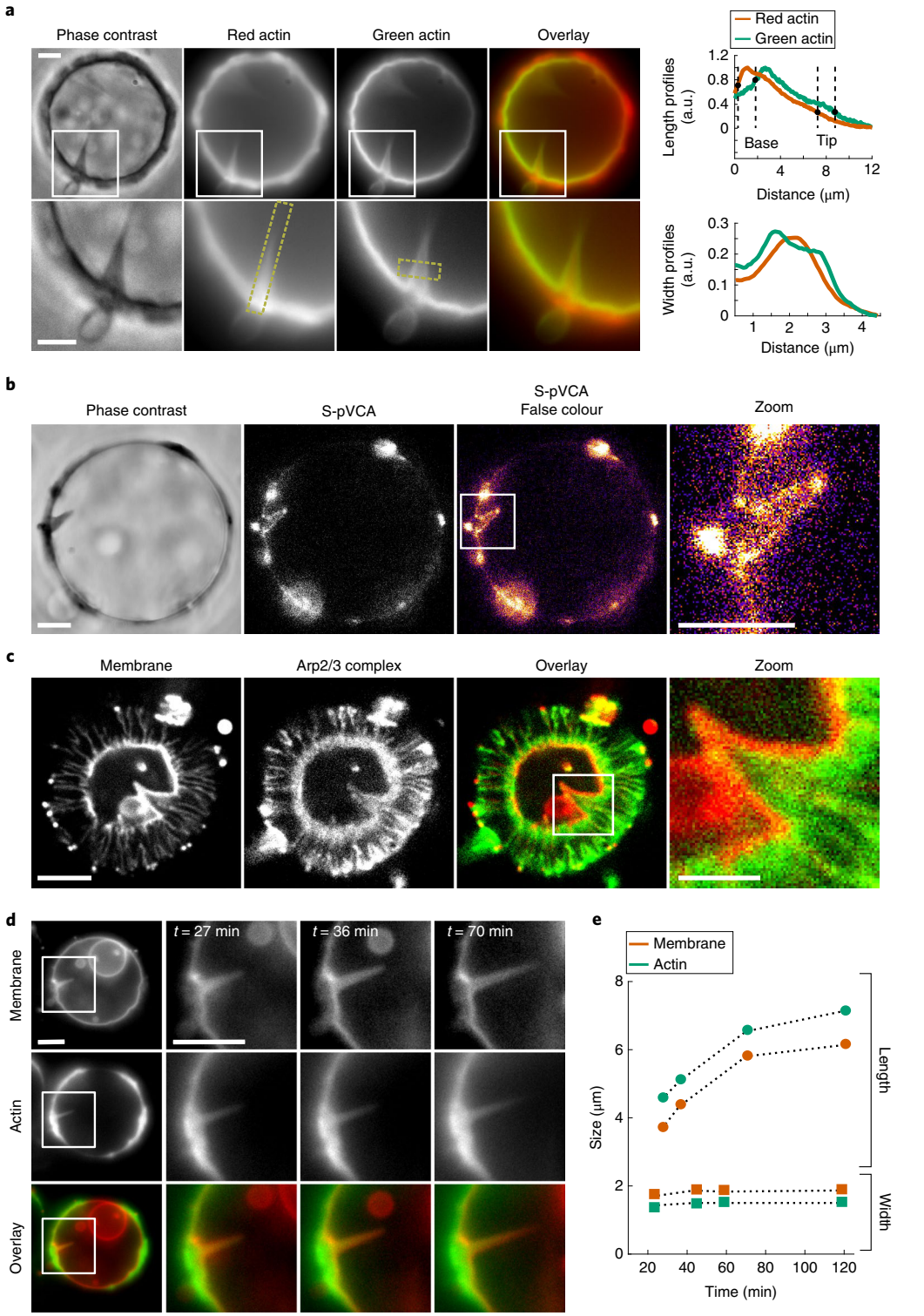

Fig. 4 | Actin incorporation in spikes. a, Left: two-colour experiment; green regions indicate newly polymerized actin. White squares, zooms. Right: fluorescence intensity profiles of spike length (top, yellow dashed box displayed on zoomed image of red actin) and width (bottom, yellow dashed box displayed on zoomed image of green actin). **b**, Activator of actin polymerization, S-pVCA. False-colour image and zoom in (white rectangle). **a**,**b**, Phase-contrast and epifluorescence microscopy of the actin network labelled with Alexa Fluor 568 (red) and Alexa Fluor 488 (green) (**a**), and S-pVCA–Alexa Fluor 546 (**b**). **c**, Confocal images of labelled membrane (Texas Red-DHPE, red) and the Arp2/3 complex (Alexa Fluor 488 C_5-maleimide, green) and zoom in (white rectangle). **d**, Epifluorescence images of membrane (Texas Red-DHPE, red) and actin (Alexa Fluor 488, green) during spike growth, as a function of time (the time indicated is that after actin polymerization starts). **e**, Spike length and width over time; spike shown in **d**. Other examples are given in Supplementary Fig. 8. The dashed lines are guides to the eyes. All scale bars, 5 μm.

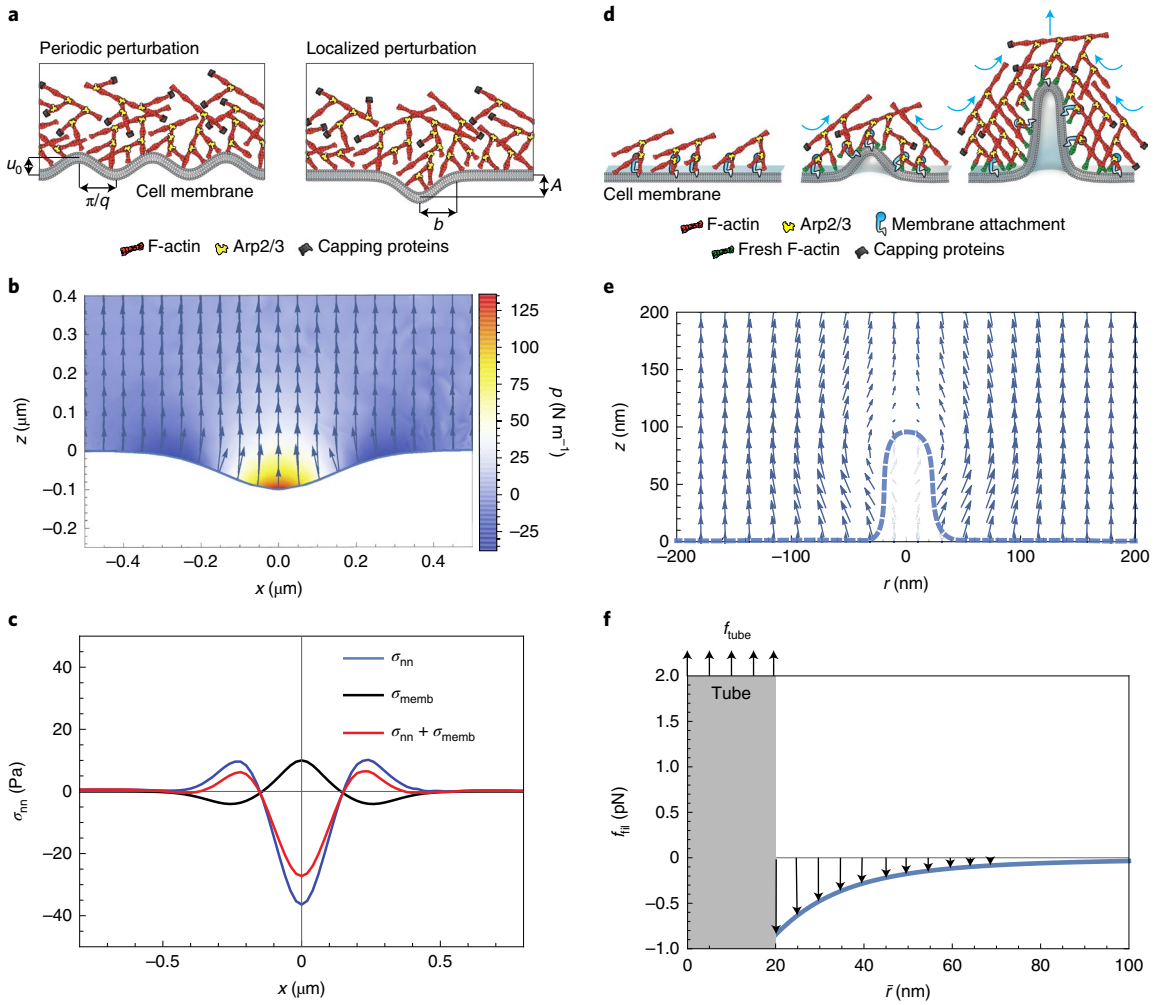

Fig. 5 | Model for spike initiation and tube formation. a, Scheme of the initiation of a periodic and localized membrane deformation by the growth of the actin network. **b**, Velocity field of a viscous network polymerizing over a membrane with a localized (Gaussian) perturbation (amplitude $A = 0.1\,\mu m$, width $b = 0.2\,\mu m$, polymerization velocity $v_g = 1\,nm\,s^{-1}$, viscosity $\eta = 10^4\,Pa\,s$). Colour, pressure in the network layer. **c**, Corresponding distribution of actin and membrane normal stresses (σ_{nn} and σ_{memb}, respectively). **d**, Scheme of a membrane tube pulled by the actin network; the blue arrows indicate forces within the actin network. **e**, Velocity field of the actin network pulling the membrane tube. We assume a uniform polymerization v_p at the liposome surface and model the presence of the tube as a disc with radius $r_{tube} = 20\,nm$ at a distance from the membrane $h = 100\,nm$. **f**, Force exerted per filament as a function of the distance to the centre of the tube, $\bar{r}$, where we have chosen the distance between filaments polymerizing on the surface $\xi = 30\,nm$, $f_{tube} = 2\,pN$, $\gamma = 10^{-6}\,N\,m^{-1}$ and $\nu = 0.4$.

time (τ_{ve}): $\eta \approx E\tau_{ve} \approx 10^4\,Pa\,s$ (with $E \approx 10^4\,Pa$ (ref. [20]) and $\tau_{ve} \approx 1\,s$ (refs. [14,15])), $\kappa \approx 10\,k_BT$ and $v_g \approx 10^{-9}\,m\,s^{-1}$ (Fig. 3d, note that this velocity is lower than the polymerization of a single actin filament because the network grows under stress[16]), we find $\gamma^* \approx 10^{-6}\,N\,m^{-1}$. This value is in the range of membrane tension for non-deflated liposomes[21], but is larger than the tension of deflated liposomes, leading to the prediction that deflated liposomes are prone to the formation of spikes, in agreement with our experimental results (Fig. 1c). Spike initiation also depends on the structure of the actin network through the value of the network viscosity η. Using the relationship[22] $\eta \approx k_BTl_p\tau_{ve}/\xi^4$, with l_p being the persistence length of the actin filament (~10 μm)[23], we find the following condition for spike initiation:

$$\gamma\xi^4 < k_BTl_pv_g\tau_{ve}\sqrt{\frac{k_BT}{2\pi\kappa}} \quad (1)$$

In contrast to 'thin' spike-like protrusions[6], the spikes we consider here are formed by the growth of a branched network with a uniform polymerization along the liposome membrane (Fig. 4). The compressive stress resulting from actin polymerization (shown in Fig. 5b) explains that spikes are much wider than the ones previously observed[6], and that they grow faster than the surrounding actin layer (Supplementary Information and Fig. 4).

The initiation of membrane tubes in the reference condition requires a pulling force at the tip of the tube larger than $f_{tube} = 2\pi\sqrt{2\kappa\gamma} \approx 2$ pN (refs. [24,25]; Fig. 5d with the above estimates). The tube radius ($r_{tube} = \sqrt{\kappa/(2\gamma)} \approx 20$ nm) is smaller than the size of the actin mesh through which it is pulled. This situation differs from spikes where the flow of the actin network is enslaved to the shape of the membrane, thus generating a wider deformation. In our case, tube pulling requires physical attachment of the actin to the membrane through the activator pVCA[26].

The force exerted by the growth of the actin network (moving away from the liposome surface at a velocity v_g) on the filament bound to the tip of the tube (moving at a velocity $\dot{L}$) is equivalent to a friction force (Supplementary Information), which can be crudely estimated using the Stokes law: $f_{drag} = 6\pi\eta r_{tube}(v_g - \dot{L})$ (Fig. 5e). At steady state, this force has to balance the tube force

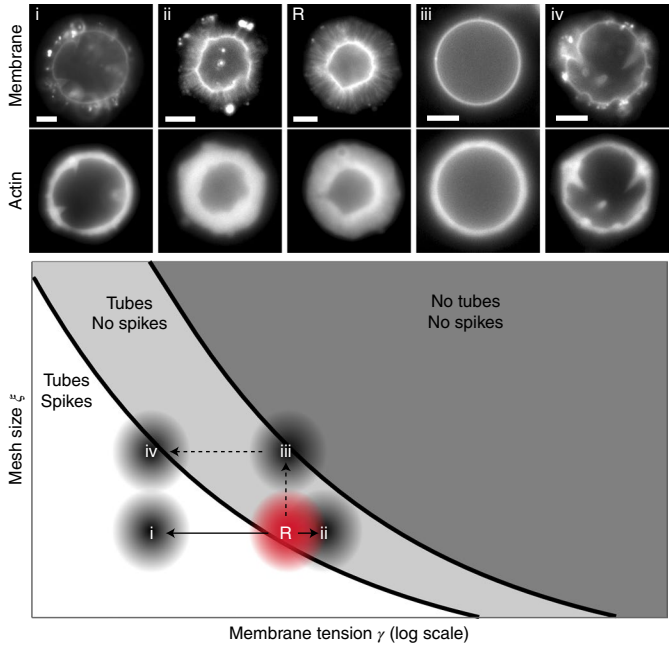

Fig. 6 | Dependence of membrane deformations on membrane tension and actin network mesh size. Representative images of membrane (Texas Red-DHPE) and actin (Alexa Fluor 488) and schematic of membrane deformations as a function of mesh size ξ and membrane tension γ, derived from the theoretical model (equations (1) and (2)). R corresponds to reference conditions (dense network, non-deflated liposomes, red dot in diagram); i, ii, iii and iv correspond to other experimental conditions with a different mesh size and membrane tension indicated qualitatively in the diagram. The arrows show in which direction membrane tension or mesh size is changed compared with the reference situation (R). The plain arrows indicate a change in membrane tension without affecting the polymerization conditions. The dashed arrows indicate that the conditions of actin polymerization are changed compared to the reference condition. All scale bars, 5 µm.

f_{tube} (Fig. 5f), giving the tube extraction velocity $\dot{L} = v_{\mathrm{g}}\left(1-\frac{f_{\mathrm{tube}}}{6\,\pi\eta r_{\mathrm{tube}} v_{\mathrm{g}}}\right)$. Tube extraction is possible provided $\dot{L} > 0$. This is indeed the case for liposomes under reference conditions ($\gamma \approx 10^{-6}\,\mathrm{N\,m^{-1}}$), for which $6\pi\eta r_{\mathrm{tube}} v_{\mathrm{g}} = 6\pi\eta\left(\frac{f_{\mathrm{tube}}}{4\pi\gamma}\right)v_{\mathrm{g}} = \frac{3\eta v_{\mathrm{g}}}{2\gamma} f_{\mathrm{tube}} \approx 10 f_{\mathrm{tube}}$ (with the above estimates). Note that $\dot{L} \gtrsim 0.9 v_{\mathrm{g}}$, explaining why tubes initiated early during actin growth actually span the entire actin layer. A tenfold increase of membrane tension could in principle prevent tube formation. Hypo-tonic treatment does not change the occurrence of tubes (Supplementary Fig. 1c), suggesting that the tension does not reach a sufficiently high level under these conditions. Using the relationship[22] $\eta \approx k_{\mathrm{B}} T l_{\mathrm{p}} \tau_{\mathrm{ve}} / \xi^4$ the condition for tube extraction is:

$$\gamma \xi^4 < \frac{3}{2} k_{\mathrm{B}} T l_{\mathrm{p}} v_{\mathrm{g}} \tau_{\mathrm{ve}} \qquad (2)$$

(Supplementary Fig. 10d). Increasing the actin mesh size indeed significantly reduces the occurrence of membrane tubes (Supplementary Fig. 9). Omitting CP, in principle, also decreases network mesh size, and no membrane tubes have been reported in these conditions[6,27]. In yeast, actin is absolutely required for endocytosis, probably because of the high turgor pressure that opposes inward membrane deformations[28–30]. The force needed to overcome the turgor pressure can reach 1,000 pN[31], almost three orders of magnitude larger than the actin force in our in vitro conditions. Using yeast-relevant parameters for actin dynamics (polymerization velocity $v_{\mathrm{p}} = 50\,\mathrm{nm\,s^{-1}}$ (ref. [1]) and actin network viscosity $\eta = 10^5\,\mathrm{Pa\,s}$ as estimated from the same scaling law as above and with a Young's modulus $E \approx 10^4\,\mathrm{Pa}$, for an actin network in cell extracts[32] and $\tau_{\mathrm{ve}} \approx 10\,\mathrm{s}$), the drag force generated by the actin network on a tube of radius $r = 10\,\mathrm{nm}$ is on the nanoNewton order. It is thus in principle able to overcome the turgor pressure and to trigger membrane deformation leading to endocytosis (Supplementary Information).

The cell is a robust system where redundant mechanisms ensure proper function, which makes detailed cell mechanisms difficult to decipher. This is true for membrane deformations into filopodia[5] or endocytic intermediates[1]. Here, we show that a branched actin network growing at a membrane is able to mimic the initiation of either an endocytosis-like or a dendritic filopodia-like deformation. Our results support recent findings that the initiation of dendritic filopodia and endocytosis primarily relies on the growth of a branched actin network[1,3,5].

Endocytosis is intimately dependent on the existence of a physical link between the actin network and the plasma membrane in yeast as well as in mammalian cells under high cell tension. Controlled endocytosis is abolished in yeast if this link is suppressed, although already endocytosed vesicles retain their extraordinary capacity to polymerize actin and even undergo actin-based motility[3,33]. In our reconstituted system, the membrane–pVCA–network linkage is essential to produce tubes, as the absence of one of these links precludes tubular membrane deformation (Supplementary Information, Supplementary Fig. 2a and Fig. 5d). In fact, the pVCA region interacts with branched actin networks both through the binding of the Arp2/3 complex[26] and through tethering of actin filament free barbed ends[34]. Note that another form of pVCA was shown to induce clustering and phase separation of lipids in the absence of CP, but not membrane deformations[26]. Here we show that, through our membrane–pVCA–network linkage, actin dynamics alone have the remarkable capacity to initiate endocytosis-like membrane deformations with a width smaller than, or of the order of, the actin mesh size.

A class of model for filopodia initiation assumes a particular actin organization in the protrusion, typically that of bundled actin filaments[6,17,18,35,36]. Supported by our dual-colour actin measurements and by labelling of the Arp2/3 complex and CP, our model for spike initiation assumes that actin polymerization occurs uniformly at the membrane, which indicates that new actin is incorporated all along the conical membrane surface, and not only at the tip of the protrusion as observed by Liu et al.[6]. Moreover, our characterization reveals that the actin network is branched during the entire growth process. Decreasing membrane tension decreases the critical amplitude for spike nucleation and increases the likelihood of spike formation (Fig. 6) oppositely to thin actin filament protrusions[6], thus revealing the very different nature of these two types of protrusion, both in their initiation, and in their subsequent growth dynamics. Spikes are mimics of filopodia, especially in the case of dendritic filopodia whose formation relies on the Arp2/3 complex-branched network[37].

Our experimental and theoretical results are summarized in Fig. 6, where the thresholds for spike and tube formation (equations (1) and (2)) are shown together with the explored experimental conditions. We conclude that tubes and spikes coexist at low tension or low mesh size whereas we predict that they do not form at high tension and high mesh size. At intermediate tension and mesh size, only tubes form, but not spikes. We thus highlight how membrane deformations induced by actin polymerization can be modulated by the interplay between membrane tension and actin network mesh size.

Online content

Any methods, additional references, Nature Research reporting summaries, source data, statements of data availability and associated accession codes are available at https://doi.org/10.1038/s41567-019-0464-1.

Received: 28 March 2018; Accepted: 8 February 2019;
Published online: 18 March 2019

References

1. Kukulski, W., Schorb, M., Kaksonen, M. & Briggs, J. A. Plasma membrane reshaping during endocytosis is revealed by time-resolved electron tomography. *Cell* **150**, 508–520 (2012).
2. Picco, A., Mund, M., Ries, J., Nedelec, F. & Kaksonen, M. Visualizing the functional architecture of the endocytic machinery. *Elife* **4**, e04535 (2015).
3. Picco, A. et al. The contributions of the actin machinery to endocytic membrane bending and vesicle formation. *Mol. Biol. Cell* **29**, 1346–1358 (2018).
4. Boulant, S., Kural, C., Zeeh, J. C., Ubelmann, F. & Kirchhausen, T. Actin dynamics counteract membrane tension during clathrin-mediated endocytosis. *Nat. Cell Biol.* **13**, 1124–1131 (2011).
5. Korobova, F. & Svitkina, T. Molecular architecture of synaptic actin cytoskeleton in hippocampal neurons reveals a mechanism of dendritic spine morphogenesis. *Mol. Biol. Cell* **21**, 165–176 (2010).
6. Liu, A. P. et al. Membrane induced bundling of actin filaments. *Nat. Phys.* **4**, 789–793 (2008).
7. van der Gucht, J., Paluch, E., Plastino, J. & Sykes, C. Stress release drives symmetry breaking for actin-based movement. *Proc. Natl Acad. Sci. USA* **102**, 7847–7852 (2005).
8. Carvalho, K. et al. Actin polymerization or myosin contraction: two ways to build up cortical tension for symmetry breaking. *Phil. Trans. R. Soc. B* **368**, 20130005 (2013).
9. Paluch, E., Piel, M., Prost, J., Bornens, M. & Sykes, C. Cortical actomyosin breakage triggers shape oscillations in cells and cell fragments. *Biophys. J.* **89**, 724–733 (2005).
10. Akin, O. & Mullins, R. D. Capping protein increases the rate of actin-based motility by promoting filament nucleation by the Arp2/3 complex. *Cell* **133**, 841–851 (2008).
11. Kawska, A. et al. How actin network dynamics control the onset of actin-based motility. *Proc. Natl Acad. Sci. USA* **109**, 14440–14445 (2012).
12. Pernier, J., Shekhar, S., Jegou, A., Guichard, B. & Carlier, M.-F. Profilin interaction with actin filament barbed end controls dynamic instability. *Dev. Cell* **36**, 201–214 (2016).
13. Julicher, F., Kruse, K., Prost, J. & Joanny, J. F. Active behavior of the cytoskeleton. *Phys. Rep.* **449**, 3–28 (2007).
14. Gardel, M. L. et al. Scaling of F-actin network rheology to probe single filament elasticity and dynamics. *Phys. Rev. Lett.* **93**, 188102 (2004).
15. Gardel, M. L., Kasza, K. E., Brangwynne, C. P., Liu, J. & Weitz, D. A. Chapter 19: Mechanical response of cytoskeletal networks. *Methods Cell Biol.* **89**, 487–519 (2008).
16. Noireaux, V. et al. Growing an actin gel on spherical surfaces. *Biophys. J.* **78**, 1643–1654 (2000).
17. Mogilner, A. & Rubinstein, B. The physics of filopodial protrusion. *Biophys. J.* **89**, 782–795 (2005).
18. Prost, J., Barbetta, C. & Joanny, J. F. Dynamical control of the shape and size of stereocilia and microvilli. *Biophys. J.* **93**, 1124–1133 (2007).
19. Deserno, M. Fluid lipid membranes: from differential geometry to curvature stresses. *Chem. Phys. Lipids* **185**, 11–45 (2015).
20. Marcy, Y., Prost, J., Carlier, M.-F. & Sykes, C. Forces generated during actin-based propulsion: a direct measurement by micromanipulation. *Proc. Natl Acad. Sci. USA* **101**, 5993–5997 (2004).
21. Caorsi, V. et al. Cell-sized liposome doublets reveal active tension build-up driven by acto-myosin dynamics. *Soft Matter* **12**, 6223–6231 (2016).
22. Kroy, K. & Frey, E. Force-extension relation and plateau modulus for wormlike chains. *Phys. Rev. Lett.* **77**, 306–309 (1996).
23. Isambert, H. et al. Flexibility of actin filaments derived from thermal fluctuations. *J. Biol. Chem.* **270**, 11437–11444 (1995).
24. Derenyi, I., Julicher, F. & Prost, J. Formation and interaction of membrane tubes. *Phys. Rev. Lett.* **88**, 238101 (2002).
25. Roux, A. et al. Role of curvature and phase transition in lipid sorting and fission of membrane tubules. *EMBO J.* **24**, 1537–1545 (2005).
26. Smith, B. A. et al. Three-color single molecule imaging shows WASP detachment from Arp2/3 complex triggers actin filament branch formation. *Elife* **2**, e01008 (2013).
27. Liu, A. P. & Fletcher, D. A. Actin polymerization serves as a membrane domain switch in model lipid bilayers. *Biophys. J.* **91**, 4064–4070 (2006).
28. Wang, X. & Carlsson, A. E. A master equation approach to actin polymerization applied to endocytosis in yeast. *PLoS Comput. Biol.* **13**, e1005901 (2017).
29. Carlsson, A. E. Membrane bending by actin polymerization. *Curr. Opin. Cell Biol.* **50**, 1–7 (2017).
30. Aghamohammadzadeh, S. & Ayscough, K. R. Differential requirements for actin during yeast and mammalian endocytosis. *Nat. Cell Biol.* **11**, 1039–1042 (2009).
31. Dmitrieff, S. & Nedelec, F. Membrane mechanics of endocytosis in cells with turgor. *PLoS Comput. Biol.* **11**, e1004538 (2015).
32. Gerbal, F., Chaikin, P., Rabin, Y. & Prost, J. An elastic analysis of *Listeria monocytogenes* propulsion. *Biophys. J.* **79**, 2259 (2000).
33. Sun, Y. et al. Switch-like Arp2/3 activation upon WASP and WIP recruitment to an apparent threshold level by multivalent linker proteins in vivo. *Elife* **6**, e29140 (2017).
34. Co, C., Wong, D., Gierke, S., Chang, V. & Taunton, J. Mechanism of actin network attachment to moving membranes: barbed end capture by. *Cell* **128**, 901–913 (2007).
35. Lan, Y. & Papoian, G. A. The stochastic dynamics of filopodial growth. *Biophys. J.* **94**, 3839–3852 (2008).
36. Atilgan, E., Wirtz, D. & Sun, S. X. Mechanics and dynamics of actin-driven thin membrane protrusions. *Biophys. J.* **90**, 65–76 (2006).
37. Hotulainen, P. et al. Defining mechanisms of actin polymerization and depolymerization during dendritic spine morphogenesis. *J. Cell Biol.* **185**, 323–339 (2009).

Acknowledgements

We acknowledge A. Kawska at IlluScientia.com for the figures. We thank J. Pernier for suggesting the excess profiling experiment for loosening the actin network. This work was supported by the French Agence Nationale pour la Recherche (ANR), grants ANR 09BLAN0283 and ANR 12BSV5001401, by Fondation pour la Recherche Médicale, grant DEQ20120323737, by the LabEx CelTisPhyBio postdoctoral fellowship (M.L.), no. ANR-10-LBX-0038 part of the IDEX PSL NANR- 10-IDEX-0001-02 PSL, by Marie Curie Integration Grant PCIG12-GA-2012-334053, 'Investissements d'Avenir' LabEx PALM (ANR-10-LABX-0039-PALM), ANR grant ANR-15-CE13-0004-03 and ERC Starting Grant 677532. Our groups belong to the CNRS consortium CellTiss. This work was supported by grants from the French National Research Agency through the 'Investments for the Future' (France-BioImaging, ANR-10-INSB-04), the PICT-IBiSA Institut Curie (Paris, France).

Author contributions

C.S., R.K. and V.C. have equal contributions. C.S. and V.C. performed experiments and analysed data. R.K. performed the development of theoretical models. A.A. M.A.-G., J.M., A.D.C., D.L., C.C. and J.P. contributed to experimental data; M.L. and J.-F.J. contributed to the development of the model; P.S. and C.S. designed the research. All authors contributed to writing the paper.

Competing interests

The authors declare no competing interests.

Additional information

Supplementary information is available for this paper at https://doi.org/10.1038/s41567-019-0464-1.

Reprints and permissions information is available at www.nature.com/reprints.

Correspondence and requests for materials should be addressed to P.S. or C.S.

Journal peer review information: *Nature Physics* thanks Allen Liu and the other anonymous reviewer(s) for their contribution to the peer review of this work.

Publisher's note: Springer Nature remains neutral with regard to jurisdictional claims in published maps and institutional affiliations.

Methods

Reagents, lipids and proteins. Chemicals are purchased from Sigma Aldrich unless specified otherwise. L-alpha-phosphatidylcholine (EPC), 1,2-distearoyl-*sn*-glycero-3-phosphoethanolamine-*N*-[biotinyl polyethylene glycol 2000] (biotinylated lipids), 1,2-dioleoyl-*sn*-glycero-3- [[*N*(5-amino-1-carboxypentyl) iminodiacetic acid]succinyl] nickel salt (DOGS-NTA-Ni) are purchased from Avanti polar lipids. Texas Red 1,2-dipalmitoyl-*sn*-glycero-3-phosphocholine, triethylammonium salt is from Thermofisher. Actin is purchased from Cytoskeleton and used with no further purification. Fluorescent Alexa Fluor 488 actin conjugate and Alexa Fluor 546 actin conjugate are obtained from Molecular Probes. Porcine Arp2/3 complex is purchased from Cytoskeleton and used with no further purification. Biotin is purchased from Sigma-Aldrich, diluted in dimethylsulfoxide. Mouse α1β2 CP is purified as in ref. [38]. Untagged human profilin and S-pVCA (the pVCA sequence starts at amino acid Gln 150) are purified as in ref. [8]. S-pVCA is fluorescently labelled on the amino-terminal amine with Alexa Fluor 546 at pH 6.5 for 2 h at 4 °C, desalted and then purified on a Superdex 200 column. His–pVCA–GST (GST–pVCA) is purified as for PRD–VCA–WAVE[39] and His–pVCA is essentially the same without the glutathione Sepharose step. Mouse α1β2 CP is fluorescently labelled with Alexa Fluor 488 C_5-maleimide (ratio of 1:1 protein/label) for 1 h at room temperature and then at 4 °C overnight under agitation. Porcine Arp2/3 complex is fluorescently labelled with Alexa Fluor 488 C_5-maleimide (ratio of 1:10 protein/label) at pH 7.2 for 3 h on ice and then purified on a PD Minitrap G-25 column.

A solution of 30 μM monomeric actin containing 15% of labelled Alexa Fluor 488 actin conjugate is obtained by incubating the actin solution in G-Buffer (2 mM Tris, 0.2 mM $CaCl_2$, 0.2 mM dithiothreitol (DTT), 0.2 mM ATP, pH 8.0) overnight at 4 °C. All proteins (S-pVCA, profilin, CP, actin) are mixed in the isotonic, hypertonic or hypotonic working buffer. The isotonic working buffer contains 25 mM imidazole, 70 mM sucrose, 1 mM Tris, 50 mM KCl, 2 mM $MgCl_2$, 0.1 mM DTT, 1.6 mM ATP, 0.02 mg ml^{-1} β-casein, adjusted to pH 7.4. The hypertonic, isotonic and hypotonic working buffers differ only by their sucrose concentration (hypertonic: 320 mM sucrose; isotonic: 70 mM sucrose; hypotonic: no sucrose). Osmolarities of the hypertonic, isotonic and hypotonic working buffers are respectively 400, 200 and 95 mOsmol, as measured with a vapour pressure osmometer (VAPRO 5600). In the case of experiments with DOGS-NTA-Ni lipids, all proteins are diluted in a working buffer containing 280 mM glucose, 10 mM HEPES, 0.5 mM DABCO, 100 mM KCl, 4 mM $MgCl_2$, 1 mM DTT, 10 mM ATP and 0.05 mg ml^{-1} β-casein.

Liposome preparation. Liposomes are prepared using the electroformation technique. Briefly, 10 μl of a mixture of EPC lipids, 0.1% biotinylated lipids or 5% DOGS-NTA-Ni lipids, and 0.1% Texas Red lipids with a concentration of 2.5 mg ml^{-1} in chloroform/methanol 5:3 (v/v) are spread onto indium tin oxide (ITO)-coated plates under vacuum for 2 h. A chamber is formed using the ITO plates (their conductive sides facing each other) filled with a sucrose buffer (0.2 M sucrose, 2 mM Tris-adjusted at pH 7.4) and sealed with haematocrit paste (Vitrex Medical). Liposomes are formed by applying an alternating current voltage (10 Hz, 1 V) for 2 h. Liposomes are then incubated with an activator of actin polymerization (S-pVCA, 350 nM) via a streptavidin–biotin link for 15 min. Isotonic liposomes are used right away for polymerizing actin in the isotonic working buffer. To obtain deflated or tense liposomes, an extra step is added: they are diluted twice in the hypertonic (400 mOsmol) or hypotonic (95 mOsmol) working buffer respectively and incubated for 30 min. The final solution is therefore at 300 mOsmol or 110 mOsmol respectively.

Biotin-blocking experiments. S-pVCA labelled with Alexa Fluor 546 and biotin are diluted in the isotonic working buffer and incubated for 10 min to reach a final concentration of 350 nM S-pVCA and various concentrations of biotin (87.5 nM, 175 nM, 262.5 nM, 350 nM). Note that 350 nM of biotin corresponds to a full saturation of the streptavidin sites of S-pVCA. Unlabelled liposomes (99.9% EPC lipids, 0.1% biotinylated lipids) are then diluted twice in this solution and incubated for 15 min. Tubes and spikes are visualized by the fluorescence of S-pVCA.

Actin cortices with a branched network. Our condition of reference ('reference condition') corresponds to condition 1 and non-deflated liposomes.

In condition 1, actin polymerization is triggered by diluting the non-deflated, deflated or tense liposomes 6 times in a mix of respectively isotonic, hypertonic or hypotonic working buffer containing final concentrations of 3 μM monomeric actin (15% fluorescently labelled with Alexa Fluor 488), 3 μM profilin, 37 nM Arp2/3 complex, 25 nM CP. Note that the final concentrations of salt and ATP in all conditions (isotonic, hypertonic, hypotonic) are 0.3 mM NaCl, 41 mM KCl, 1.6 mM $MgCl_2$, 0.02 mM $CaCl_2$ and 1.5 mM ATP.

Condition 2 follows the same protocol as in condition 1 with unlabelled monomeric actin, unlabelled liposomes (99.9% EPC lipids, 0.1% biotinylated lipids) and S-pVCA labelled with Alexa Fluor 546.

In Fig. 1c, non-deflated liposomes $n = 311$ are distributed as follows: 215 from 3 experiments in condition 1 and 96 from 2 experiments in condition 2. Deflated liposomes $n = 123$ are distributed as follows: 92 from 2 experiments in condition 1 and 31 from 1 experiment in condition 2.

Condition 3 follows the same protocol as in condition 1 with unlabelled monomeric actin and Arp2/3 complex labelled with Alexa Fluor 488 C_5-maleimide.

Condition 4 follows the same protocol as in condition 1 with unlabelled monomeric actin and CP labelled with Alexa Fluor 488 C_5-maleimide.

Actin cortices with a loosened branched network. Actin polymerization is triggered the same way as above (condition 1), except with 15 μM profilin (instead of 3), and during a longer time (overnight instead of 1–2 h). Reference conditions correspond to non-deflated liposomes in condition 1, except that observation is performed 20 h after the initiation of polymerization.

Photo-damage of the actin network. The actin network area to photo-damage is defined with a diaphragm. The area is illuminated for 15 s with a Hg lamp and a FITC filter cube and the illumination is repeated until the actin is completely destroyed or at least no longer detectable by eye.

Two-colour experiment. Liposomes are first incubated with 350 nM S-pVCA for 15 min. This solution is then diluted threefold into a mix of isotonic buffer containing 3 μM actin (15% Alexa568-labelled, red), 37 nM Arp2/3 complex and 25 nM CP. After 20 min of incubation in these conditions, the solution is diluted 3 times in a mix of the same protein concentrations containing 15% Alexa488-labelled actin, green.

Free actin filament barbed end labelling. S-pVCA-activated liposomes (labelled membrane) are placed in a mix containing 3 μM unlabelled monomeric actin, 37 nM unlabelled Arp2/3 complex and 25 nM unlabelled CP. After 20 min of incubation in these conditions, the solution is diluted 5 times in the working buffer to stop actin polymerization. This solution is then incubated with 75 nM labelled CP. Image acquisition is performed right after the addition of fluorescently labelled CP.

Cryo-electron microscopy. To prepare small liposomes, a mixture of EPC lipids and 0.1% biotinylated lipids with a concentration of 1 mg ml^{-1} in chloroform/methanol 5:3 (v/v) is dried and resuspended under vortexing in a buffer containing 25 mM imidazole, 1 mM Tris, 50 mM KCl, 2 mM $MgCl_2$, 0.1 mM DTT, 1.6 mM ATP and 0.02 mg ml^{-1} β-casein. Liposomes are then incubated with S-pVCA (350 nM) for 15 min and finally flash-frozen for cryo-electron microscopy. Images were recorded under low-dose conditions with a Tecnai G2 Lab6 electron microscope operating at 200 kV with a TVIPS F416 4K camera and with a resolution of 0.21 Å per pixel.

Observation of liposomes. For observation in two dimensions, epifluorescence (GFP filter cube, excitation 470 nm, emission 525 nm; Texas Red filter cube: excitation 545–580 nm, emission 610 nm-IR), phase-contrast and bright-field microscopy are performed using an IX70 Olympus inverted microscope with a 100× or a 60× oil-immersion objective. Images are collected by a CCD (charge-coupled device) camera (CoolSnap, Photometrics, Roper Scientific).

For observation in three dimensions: confocal and bright-field microscopy are performed using an inverted confocal spinning disc Roper/Nikon with a 100× or a 60× oil-immersion objective and lasers with wavelengths of 491 nm for actin and 561 nm for lipids. A FITC filter cube (excitation filter: 478–495 nm/emission filter: 510–555 nm) and a TxRed filter cube (excitation filter: 560–580 nm/emission filter: 600–650 nm) are used to acquire respectively actin and lipids fluorescence. Images are collected by a CCD camera (CoolSnap HQ2, Photometrics, Roper Scientific).

For three-dimensional data, *z*-stacks are acquired using the software Metamorph on each wavelength with a *z*-interval of 0.5 μm.

Image analyses of liposomes, tubes and spikes. Image analyses are performed with ImageJ software and data are processed on Matlab. The thickness of the actin network and the length of the tube membranes are obtained from fluorescence intensity profiles (Fig. 3a). The first peak of the membrane profile determines the liposome surface and the second peak determines the end of the membrane tube. The actin network thickness is the distance between the first peak and the half-width at half-maximum of the actin fluorescence profile. The length of the membrane tubes is obtained as the peak-to-peak distance of the membrane fluorescence profile. The size of the spikes (length, width) and the actin network is determined by the corresponding positions of the inflexion points. Fluorescence profiles in each case (membrane, actin) are fitted with a polynomial function. The first maximum and the second minimum of the fit derivative, corresponding to inflexion points of the profile, determine the membrane or actin edges. The size is then the distance between the two edges. From the actin fluorescence profile, the actin network thickness at the base of the spike is defined as the distance between the first maximum and the first minimum of the fit derivative.

To determine whether shorter tubes are present in addition to the easily visualized long ones, we measure the total fluorescence intensity of the membrane on an arc that is displaced along a radial axis *r* from close to the liposome surface to the external part of the network. We hypothesize that tubes maintain a constant diameter along their length, as is established for pure membrane tubes[24]. In these conditions, if all tubes have the same length, the total intensity should show a plateau as a function of *r*, until falling off to zero at an *r* where there are no more

tubes (Supplementary Fig. 4a). Conversely, the total intensity would decrease as a function of r if tubes of different lengths were present (Supplementary Fig. 4a).

Statistical analyses. All statistical analyses are performed using MedCalc software. An $N-1$ chi-squared test is used to determine the statistical significance. Differences among samples were considered statistically significant when $P<0.05$.

Theoretical model for spike initiation. To calculate the stress exerted by a viscous network polymerizing at a curved surface we consider an incompressible Stokes flow, described by force balance and incompressibility; that is, $\vec{\nabla}\cdot\vec{\sigma}=0$ and $\vec{\nabla}\cdot\vec{v}=0$, where $\vec{v}$ is the velocity of the network and $\vec{\sigma}$ is the viscous stress in Cartesian coordinates, given by $\sigma_{ij}=-p\ \delta_{ij}+\eta\left(\frac{\partial v_i}{\partial x_j}+\frac{\partial v_j}{\partial x_i}\right)$. Polymerization of the actin network is encoded in this model by imposing the velocity of the network, normal to the surface of the curved interface. Moreover, we impose a stress-free boundary condition at the outer layer, both for the normal as well as the tangential stress; that is, $\sigma_{nn}=0$ and $\sigma_{nt}=0$. Note that, in the limit we consider, an infinitely thick network, this corresponds to a uniform velocity in the z-direction.

We determine the first-order correction of the normal stress on a deformed surface characterized by $u(x)=u_0\exp(iqx)$ along the x axis (u_0 is the deformation amplitude and q is the wavevector; Fig. 5a, left). We seek a solution for the velocity field within the network of the form $v_j=v_j(z)\exp(iqx)$, where the index j represents the coordinate x or z, and a pressure field of the form $p=p(z)\exp(iqx)$. Assuming that the network grows normal to the surface, the first-order correction of the x-component of the velocity field satisfies the boundary condition $\delta v_x(z=0)=-v_g\partial_x u(x)$ at the interface ($z=0$). We assume here a network of large thickness and require that the first-order correction to the velocity vanishes at $z\to\infty$. The first-order corrections to the velocity and pressure in the network read $\delta v_x(z)=-iqu_0(1-qz)v_g\exp(-qz)$, $\delta v_z(z)=-q^2u_0v_gz\exp(-qz)$ and $\delta p(z)=-2\eta q^2u_0v_g\exp(-qz)$. At this order the actin normal stress turns out to vanish at any point of the liposome surface: $\sigma_{nn}(x,z=0)=2\eta\partial_z v_z-p=0$. This implies that the membrane is linearly stable against small deformations in the presence of a growing actin network.

The second-order correction for the actin stress is in principle difficult to calculate, as the different modes of deformation are coupled. An analytical estimate can be obtained by expanding the surface normal vector up to second order, which yields the following scaling for the normal stress at the liposome surface, $\sigma_{nn}\propto-\eta q^3u_0^2v_g$. This weakly nonlinear analysis reveals that there is a non-zero normal stress acting on the membrane, which we will later compare with the membrane contribution to address system stability.

To get a numerical solution for the normal stress in a 'localized' spike-like perturbation on the interface, as opposed to the periodic one presented above, we use a finite-element method from Mathematica with default settings. We implement a geometry as described in Fig. 5a (right), where the lower surface is parametrized with a Gaussian deformation as mentioned before (that is, $u(x,z)=z-A\ \exp-\left(\frac{x}{b}\right)^2=0$) and we choose the height of the system to be much larger that the extent and amplitude of the perturbation ($h=2\,\mu$m). Note that here, b, the characteristic lateral length of the localized perturbation, is related to the wavenumber $q\approx1/b$ used for the linear analysis. To account for a constant polymerization, perpendicular to the lower surface we impose the velocity on the lower surface, that is, $\partial v(u(x,z)=0)=v_g(\partial_x u(x,z)\hat{x}+\partial_z u(x,z)\hat{z})$, where v_g is the normalized polymerization velocity, and a vanishing normal and tangential stress at the upper boundary $z=h$, that is, $\sigma_{nn}(z=h)=0$ and $\sigma_{nt}(z=h)=0$. Using this approach we find the same scaling with amplitude and width of the perturbation as found for the weakly nonlinear analysis for a sinusoidal perturbation. Note also that here, by imposing the normal velocity at the interface, a choice that is motivated by the dual-colour images in Fig. 4a, we do not impose the tangential stress on the membrane, and hence this stress has to be balanced by an in-plane viscous stress in the membrane, which at this stage we do not model. These finite-element model simulations allow us to visualize the velocity field as well as the pressure throughout the network, indicating the increase in pressure inside the local perturbation caused by the local convergence of the velocity fields (Fig. 5b).

Reporting Summary. Further information on research design is available in the Nature Research Reporting Summary linked to this article.

Data availability

The data that support the plots within this paper and other findings of this study are available from the corresponding author upon request.

References

38. Palmgren, S., Ojala, P. J., Wear, M. A., Cooper, J. A. & Lappalainen, P. Interactions with PIP2, ADP-actin monomers, and capping protein regulate the activity and localization of yeast twinfilin. *J. Cell Biol.* **155**, 251–260 (2001).
39. Havrylenko, S. et al. WAVE binds Ena/VASP for enhanced Arp2/3 complex–based actin assembly. *Mol. Biol. Cell* **26**, 55–65 (2015).

nature research

Corresponding author(s): SYKES Cécile

Reporting Summary

Nature Research wishes to improve the reproducibility of the work that we publish. This form provides structure for consistency and transparency in reporting. For further information on Nature Research policies, see Authors & Referees and the Editorial Policy Checklist.

Statistical parameters

When statistical analyses are reported, confirm that the following items are present in the relevant location (e.g. figure legend, table legend, main text, or Methods section).

n/a	Confirmed	
☐	☒	The exact sample size (*n*) for each experimental group/condition, given as a discrete number and unit of measurement
☐	☒	An indication of whether measurements were taken from distinct samples or whether the same sample was measured repeatedly
☐	☒	The statistical test(s) used AND whether they are one- or two-sided *Only common tests should be described solely by name; describe more complex techniques in the Methods section.*
☒	☐	A description of all covariates tested
☒	☐	A description of any assumptions or corrections, such as tests of normality and adjustment for multiple comparisons
☐	☒	A full description of the statistics including central tendency (e.g. means) or other basic estimates (e.g. regression coefficient) AND variation (e.g. standard deviation) or associated estimates of uncertainty (e.g. confidence intervals)
☐	☒	For null hypothesis testing, the test statistic (e.g. *F*, *t*, *r*) with confidence intervals, effect sizes, degrees of freedom and *P* value noted *Give P values as exact values whenever suitable.*
☒	☐	For Bayesian analysis, information on the choice of priors and Markov chain Monte Carlo settings
☒	☐	For hierarchical and complex designs, identification of the appropriate level for tests and full reporting of outcomes
☐	☒	Estimates of effect sizes (e.g. Cohen's *d*, Pearson's *r*), indicating how they were calculated
☒	☐	Clearly defined error bars *State explicitly what error bars represent (e.g. SD, SE, CI)*

Our web collection on statistics for biologists may be useful.

Software and code

Policy information about availability of computer code

Data collection	Metamorph V7.8.13.0; Mathematica V11
Data analysis	Matlab R2016b; Excel V14.4.1 2011, Chi-squared test: https://www.medcalc.org/calc/comparison_of_proportions.php, Image J V1.47b;

For manuscripts utilizing custom algorithms or software that are central to the research but not yet described in published literature, software must be made available to editors/reviewers upon request. We strongly encourage code deposition in a community repository (e.g. GitHub). See the Nature Research guidelines for submitting code & software for further information.

Data

Policy information about availability of data

All manuscripts must include a data availability statement. This statement should provide the following information, where applicable:

- Accession codes, unique identifiers, or web links for publicly available datasets
- A list of figures that have associated raw data
- A description of any restrictions on data availability

the datasets generated during and/or analysed during the current study are available from the corresponding author on reasonable request

Field-specific reporting

Please select the best fit for your research. If you are not sure, read the appropriate sections before making your selection.

☒ Life sciences ☐ Behavioural & social sciences ☐ Ecological, evolutionary & environmental sciences

For a reference copy of the document with all sections, see nature.com/authors/policies/ReportingSummary-flat.pdf

Life sciences study design

All studies must disclose on these points even when the disclosure is negative.

Sample size	Sample size was not pre-determined. However, our main result is that actin dynamics can deform a membrane. To address which physical parameter was important to this effect, we have compared different conditions with a Chi-squared test that gave satisfactory p-values that confirmed our direct observation.
Data exclusions	Liposomes that did not show any actin signal in fluorescence microcopy were excluded, since they were not affected by actin.
Replication	Experiments were repeated 2, 3 or 5 times and displayed the same features
Randomization	The same batch of proteins were used in all experiments. Experiments were reproducible among two experimentalists (CS and VC, co-first authors).
Blinding	Blinding was used among authors for analysis. Data collection was randomized in taking random images.

Reporting for specific materials, systems and methods

Materials & experimental systems

n/a	Involved in the study
☒	☐ Unique biological materials
☒	☐ Antibodies
☒	☐ Eukaryotic cell lines
☒	☐ Palaeontology
☒	☐ Animals and other organisms
☒	☐ Human research participants

Methods

n/a	Involved in the study
☒	☐ ChIP-seq
☒	☐ Flow cytometry
☒	☐ MRI-based neuroimaging